Ground calibration of the Chandrayaan-1 X-ray Solar Monitor (XSM)

L. Alha [a,1], J. Huovelin [a], K. Nygård [b], H. Andersson [c], E. Esko [a], C.J. Howe [d], B.J. Kellett [d], S. Narendranath [g] B.J. Maddison [d], I. A. Crawford [e], M. Grande [f], P. Shreekumar [g],

[a] *Observatory, P.O. Box 14, FI-00014 University of Helsinki, Finland*

[b] *Division of X-ray Physics, Department of Physics, P.O.Box 64, FIN-00014 University of Helsinki, Finland*

[c] *Oxford Instruments Analytical, P.O.Box 85, FIN-02631 Espoo, Finland*

[d] *Rutherford Appleton Laboratory, Chilton, Didcot, OX11 0QX, UK*

[e] *School of Earth Sciences, Birkbeck College London, London, UK*

[f] *Institute of Mathematical and Physical Sciences, University of Wales, Aberystwyth, Ceredigion SY23 3BZ, UK*

[g] *Space Astronomy and Instrumentation Division, ISRO Satellite Centre, Bangalore 560017, India*

Key words: X-ray detectors, calibration

---

[1] Corresponding author. E-Mail: alha@mappi.helsinki.fi, Tel. +358-9-19121772, Fax. +358-9-19122952.

Abstract

The Chandrayaan-1 XSM ground calibrations are introduced. The aim of these calibrations was to characterize the performance of XSM, which enables a reliable spectral analysis with the solar X-ray data. The calibrations followed an improved procedure based on our experience from the SMART-1 XSM. The most important tasks in the calibrations were determination of the energy resolution as a function of the photon energy and mapping of the detector sensitivity over the FoV (Field of View) of the sensor. The FoV map was needed to determine the obscuration factor corresponding to various pointings with respect to the Sun. We made also a sensitivity comparison test between the Chandrayaan-1 XSM FM (Flight Model) and SMART-1 XSM FS (Flight Spare). The aim of this test was to link the new XSM performance to a performance of an already known and tested former instrument. We also performed a simple test to determine the pile-up performance, and one specific test tailored for the operation of the new version of XSM. Also the first experiences on the in-flight operation are briefly described.

1 Introduction

A new XSM (X-ray Solar Monitor) began to operate on board the Indian Chandrayaan-1 space craft. This first Indian lunar mission was launched on the 22^{nd} of Oct. 2008. The observational task of this new XSM was to observe the solar X-ray emission, while the C1XS (Chandrayaan-1 X-ray Spectrometer) instrument was designed to measure the fluorescence emission from the Moon soil induced by the solar X-ray emission [1]. Chandrayaan-1 S/C (Space Craft) has by now reached its almost circular polar orbit about 200 km above the surface of the Moon.

This new XSM differs from its predecessor SMART-1 XSM [2] in three ways [3]. Firstly, the low energy sensitivity was enhanced by a thinner Be-filter having a thickness of 13μm instead of 27μm, which was used in SMART-1 XSM. Secondly, the area of the golden aperture stop hole is about 18 times smaller, to cover a wider dynamical range with respect to higher count rates during M and X-level flares. Thirdly, the sensor electronics are also equipped with a less noisy FET transistor, compared to the former XSM. All filter and detector dimensions, FoV (Field of View) geometry and technical performance values have been compiled into Table 1.

2 Ground calibrations

XSM calibrations were carried out during June 2007 in the X-ray laboratory at the University of Helsinki, Department of Physical Sciences. The X-ray laboratory has a vacuum chamber attached with a titanium X-ray tube. The lowest pressure obtained with the present two-phase rotary vane vacuum pump was 4 mbar. The inner diameter of the chamber was 630 mm and the free working height was 300 mm. The chamber consisted of an adjustable table enabling 3D-movements of the specimen. There was also a rotating goniometer inside the chamber enabling the study of FoV sensitivity at

different roll and off-axis angles. The vacuum chamber allowed measurements at soft X-ray range (E $\leq$ 5 keV). The photon energy of 5 keV is a practical low energy limit, when making measurements in a free air. The primary X-ray source of the calibration setup was a sealed and air-cooled Ti-anode miniature soft X-ray tube (Oxford X-ray Technologies Inc. model XTF-5011). This X-ray tube consists of a Be window having a thickness of 75 μm. This limits the usable soft X-ray output energies to above 1.0 keV. The tube high voltage and current were controlled manually with an accuracy of 0.1 kV (max 50 kV), and 1 μA (max 1 mA). There was also an ^{55}Fe source for operational testing, which enabled application of emission line of 5.9 keV and 6.4 keV in calibrations. The data acquisition was controlled with a special commercial software dedicated to laboratory analysis, running in the PC workstation under Linux operating system. This same software controlled the movements of the specimen. X-ray spectra were collected with a 2028 channel ISA-bus MCA (Multi Channel Analyzer) card.

2.1 Determination of the detector energy resolution as a function of a photon energy

Two different fluorescence samples and one ^{55}Fe emitter were used as emission sources. The first fluorescence sample was made of compressed powder mixtures of Al, Ca and Cu. The second sample was made of pure Pb plate. Both samples were illuminated with a titanium X-ray tube and the fluorescence emission from the samples was measured with the specimen. The specimen was also illuminated with the ^{55}Fe source in advance to get two more emission lines in the data. Both of the fluorescence samples were measured at five different detector PIN (Positive Intrinsic Negative) diode temperatures, 0°C, -5°C, -10°C, -15°C and -20°C. The integration time per spectrum with the Pb-sample was 2 hours. The respective integration time with the AlCaCu-sample was 1 hour. Table 2 and Table 3 include a list of line energies used in these energy resolution measurements. The spectra of both samples were also analyzed to determine the respective gains, offsets and line centroids. The results of this test are shown in Fig. 1. Similar plots of the fluorescence

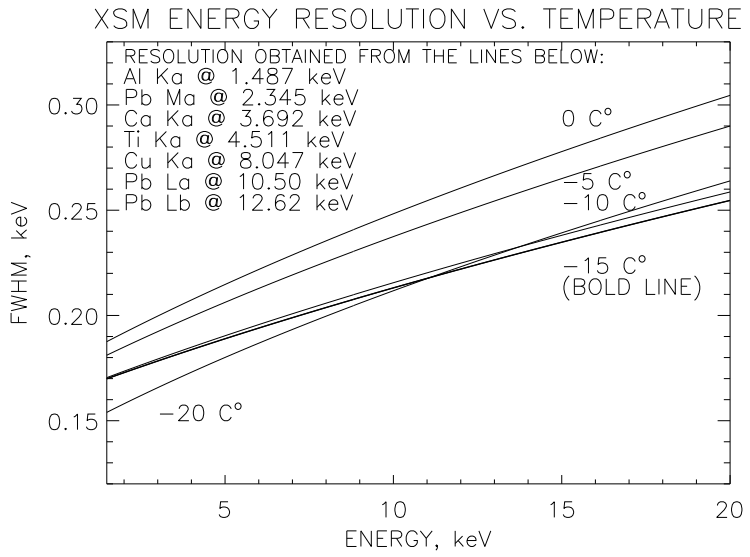

Figure 1.

spectra used in this test can be found in the section 2.4. (These plots exclude the the Mn-lines from the ^{55}Fe, which were not used in the comparison test.)

2.2 FoV (Field of View) sensitivity

The sensitivity of the detector FoV was derived as a function of two angles. These were the off-axis angle θ and the roll angle ρ. The parameter θ is the angular distance between the Sun and the detector optical axis. The (azimuthal) roll angle ρ is related to the FoV in a way shown in Fig. 3. The detector FoV corresponds to a circle having an angular radius of 52° in the celestial sphere. On the circular orbit 200 km above the Moon, the angular velocity of the Sun moving in the FoV is about 3°/min. Hence the detector sensitivity must known with an accuracy of ° 1 throughout in the FoV as a function of ρ and θ. The change of the sensitivity is caused by the dependence of the projected detector area and the shadow cast by the aperture collimator on the detector active area on the position of the light source (the Sun) in the FoV. Hence, the sensitivity is a function of ρ and θ.

The sensitivity map of the FoV was generated by illuminating the detector at different

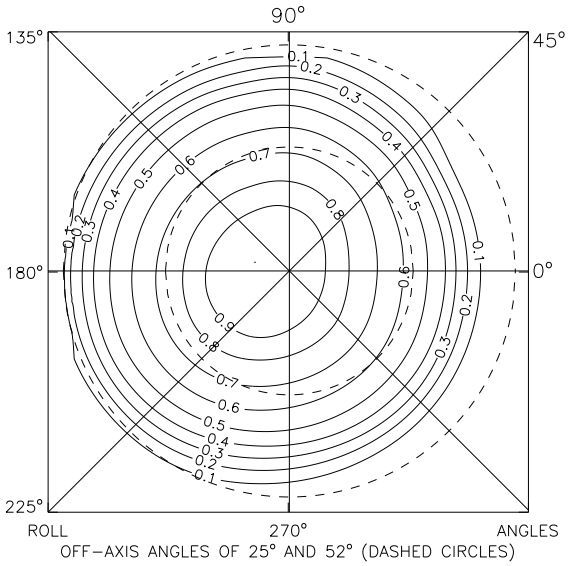

Figure 2.

angles with a constant white beam of a Ti-anode X-ray tube. A detailed description of this procedure can be found in paper [2]. The outcome of this measurement is a two-dimensional array containing obscuration factors corresponding to angle pairs of ρ and θ, which determine the position of the Sun in the detector FoV. The contour plot of this obscuration factor array is shown in Fig. 2. The test setup information related to the FoV sensitivity map is listed in Table 4.

2.3 Determination of the aperture stop diameter

The most crucial task in determining the sensitivity of a monolithic semiconductor detector is to quantify the exact size of the detector active area. This area is dictated by the stop hole aperture stop, which was machined manually by a drill bit having a nominal diameter of 0.35 mm. The edge of the aperture stop hole was found to deviate from an ideal circle by analyzing the photographs taken from under and above the machined aperture stop with a microscope. Fig. 4 illustrates the scenery taken from above the aperture stop, i.e. from the direction of the light source. As can be seen, the hole edge geometry shown in Fig. 4, is quite difficult to determine accurately. Luckily, the manufacturer had

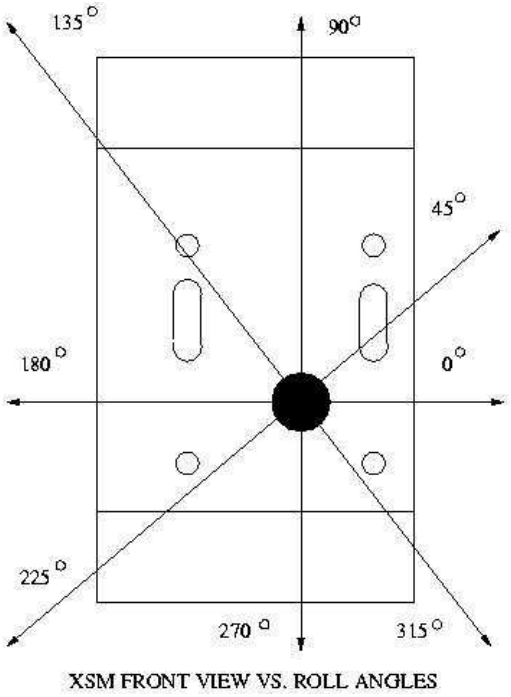

Figure 3.

included a dimensional reference scale object (i.e. a 0.35 mm drill bit) in these two jpg-formatted photos. Thus we could do a quantitative image analysis to derive the effective diameter of the drilled aperture stop hole. First we imported the photos into XFIG (a vector based drawing program running under Linux) S/W, in which we added a white color circle having an equal diameter as the drill bit. Hence, we were able to determine the metric dimensional scale of the photograph, i.e. pixel versus physical unit scale. The resulting figure was exported into a FITS-formatted file from the XFIG program and the pixel information was analyzed with the aid of the IDL^{TM} S/W in three different colors, R (Red), G (green) and B (Blue). The total number of pixels corresponding to the free entrance area of the aperture hole was calculated in three pixel colors. We obtained 6 different values for the hole areas in total (3 colors below and 3 colors above). The outcome of this photographic analysis yielded an effective diameter 0.379 mm for the Au aperture stop. The analyzed photographs illustrating the aperture stop hole in three different colors are shown in Fig. 5. The top row figures were generated with XFIG S/W. The annuli around the aperture holes were drawn in white to remove all pixels misleading the analysis. The plots in the lower row in Fig. 5 illustrate a more detailed and zoomed in

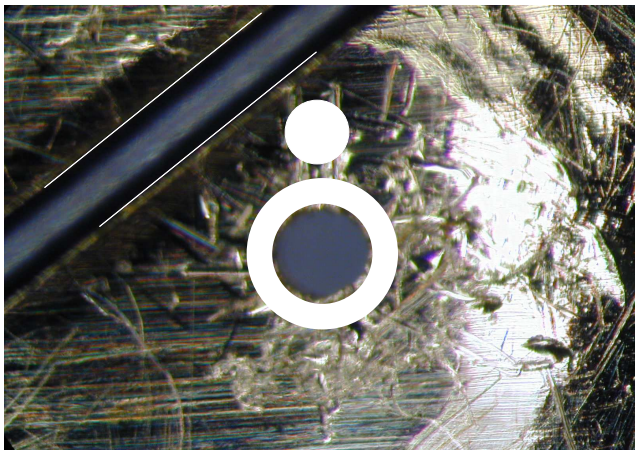

Figure 4.

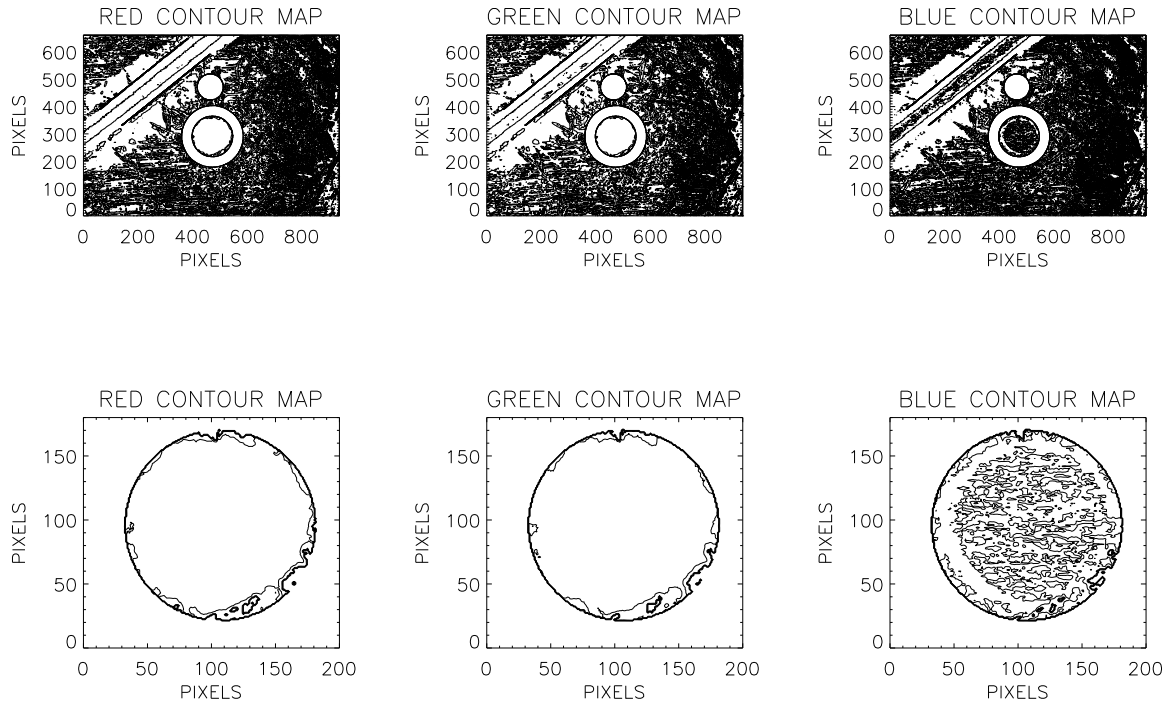

Figure 5.

areas of the manipulated photos in the respective pixel colors. (Coloring in Fig. 5 is gray.)

2.4 Comparison calibration

From the known size of Au aperture stop hole, one can determine the effective on-axis area for the detector, i.e. an ARF (Ancillary Response File) required in the spectral analysis. The QE (Quantum Efficiency) curves of the Chandrayaan-1 XSM FM and SMART-1

XSM FS are shown in Fig. 6. As can be seen, the QE-curve of the Chanrayaan-1 XSM is bit better at the low energy side due to the thinner Be-window. The plots representing the effective areas are shown in Fig. 7. The effective area of the SMART-1 XSM FS is greater due to the bigger aperture stop hole of 1.5 mm. Fig. 8 illustrates the Chanrayaan-1 XSM FM effective area calculated at the roll angle direction of 0°.

In this comparison calibration, the SMART-1 XSM FS and Chandrayaan-1 XSM FM detectors were both tested under same conditions. The test setup parameters are given in Table 5. The applied fluorescence sources used in this test were the same as in the energy resolution determination calibration explained in Section 2.4, except for excluding the Mn lines from the ^{55}Fe-source. The resulting fluorescent spectra are shown in Fig. 9 and Fig. 10. The setup parameters related to this comparison test are given in Table 5. The spectra were first fitted with the XSPEC S/W [4]. Each applied fluorescence line was fitted and the fit parameters (K_{FM} and K_{FS}) denoting the line intensities were then compared. The applied lines and numerical results are listed in Table 6. The plot in Fig. 11 illustrates the result of the comparison calibration between SMART-1 XSM FS and Chandrayaan-1 XSM FM. The SMART-1 XSM FS is an identical replica of the SMART-1 XSM FM. The latter data have been cross calibrated with the simultaneous GOES [5] (flux) data to an accuracy of about $\pm 5\%$ during the on-axis observations. For all practical purposes, this test connected the Chandrayaan-1 XSM FM sensitivity to the tested performance of previously tested detectors with known sensitivity. The sensitivity of the Chandrayaan-1 XSM FM matches quite well with the sensitivity of the SMART-1 XSM FS, which in turn represents the verified sensitivity of the SMART-1 XSM FM.

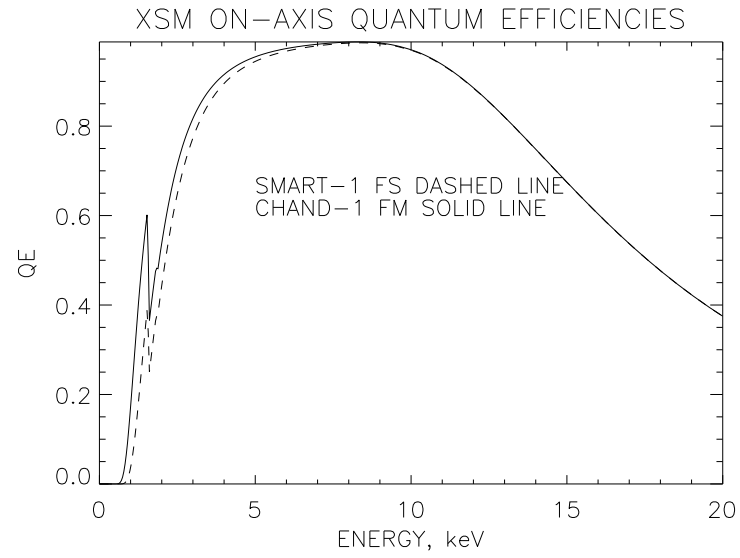

Figure 6.

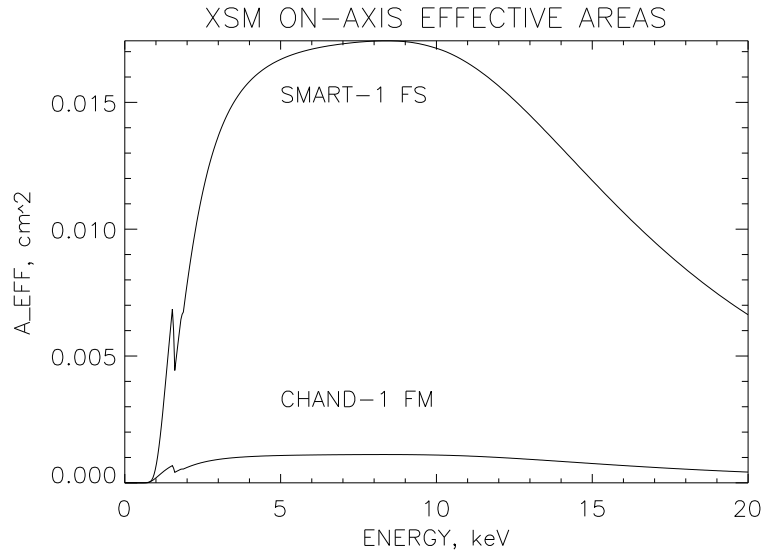

Figure 7.

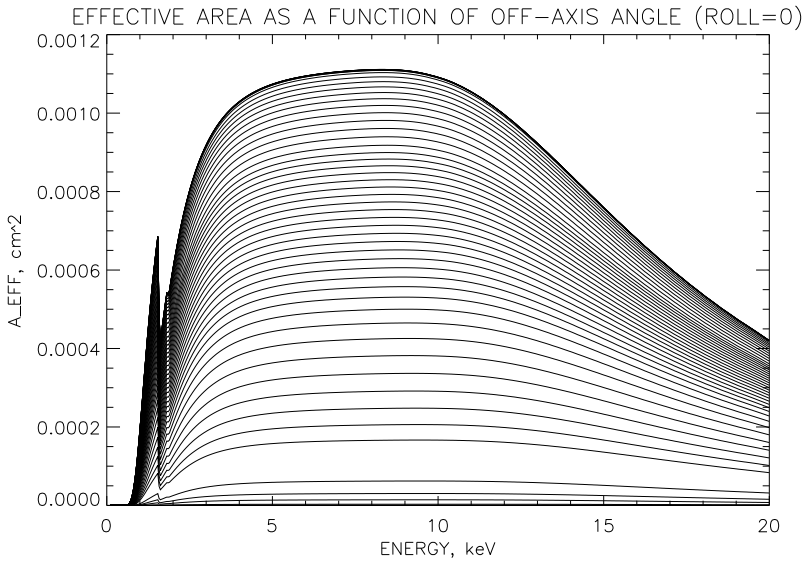

Figure 8.

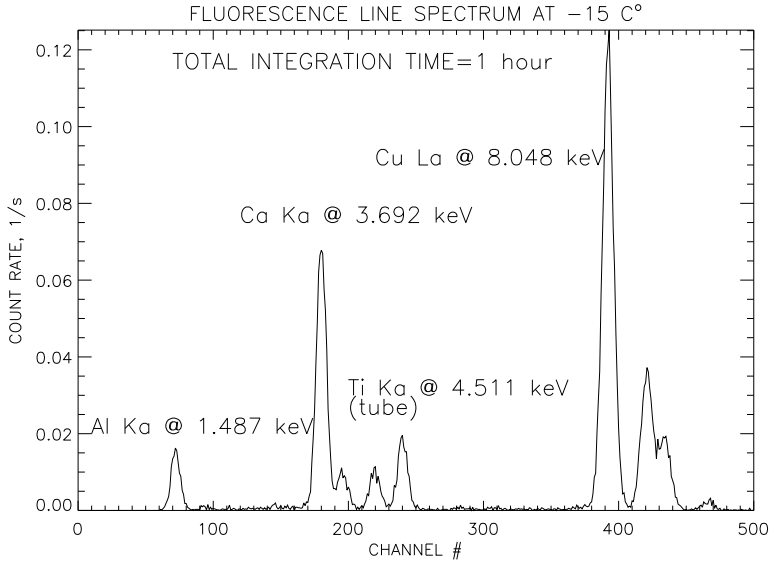

Figure 9.

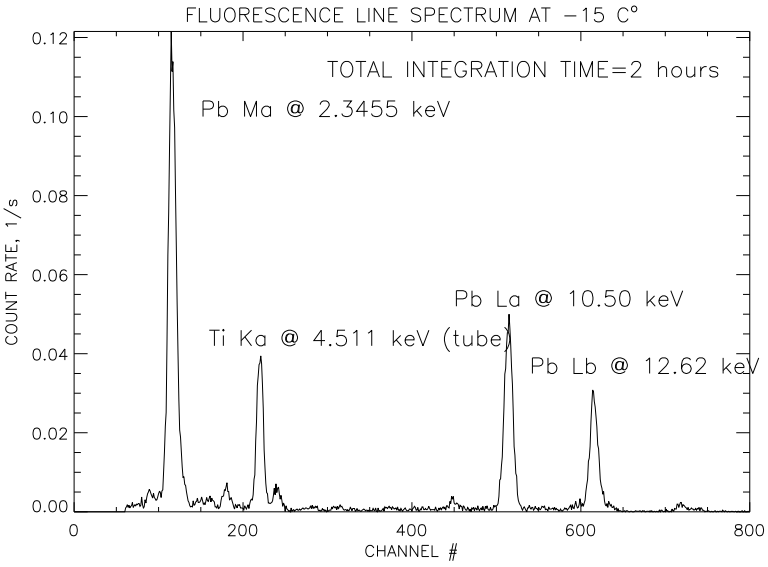

Figure 10.

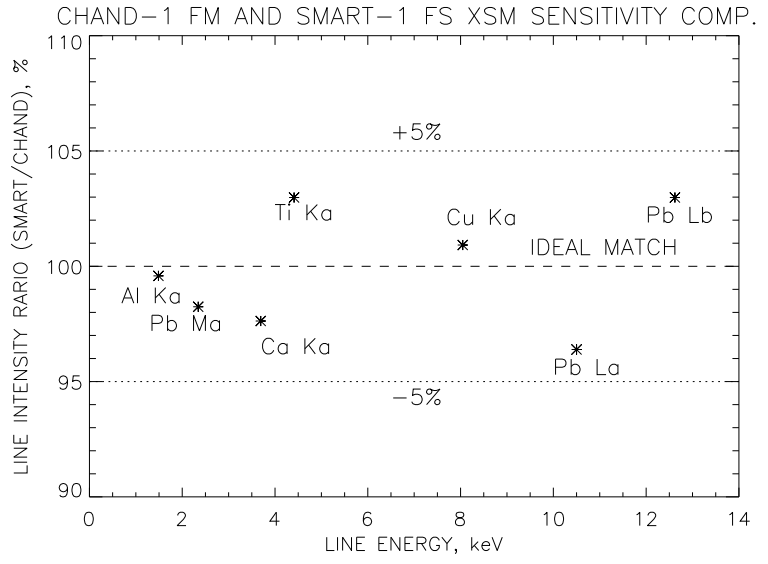

Figure 11.

2.5 Pile up test

The pile up test was carried out at the facilities of the manufacturing company, i.e. at OIA (Oxford Instruments Analytical) in Espoo, Finland. The FM electronics box was used in this test. The radiation source was an ^{55}Fe emitter with two lines at 5.9 keV and 6.5 keV. The radiation source was placed at 5 different distances from the detector to modify the recorded count rates. The closer the radiation source was to the detector, the higher was the count rate and the respective number of pile up counts. The total count rates were calculated by adding *2E* and *3E* pile up count rates with the total count rates obtained from the rest of the channels. The *2E* count rates were multiplied by a factor of two and the *3E* pile up count rates by a factor of three, which gave the intrinsic source count rates, apart from the absorption effects. The theoretical pile up curve shown in Fig. 12 includes the sum of the *2E* and *3E* pile up count rates both calculated applying Poisson statistics as shown in Eq.1.

$$Pileup = \frac{(\tau I)^n exp(-\tau I)}{n!} \tag{1}$$

The parameter n is 1 for the *2E* and 2 for the *3E* count rates. The parameter τ denotes the fast channel nominal pulse per resolution time of 2.0μs. The parameter I is the total count rate.

The calculated pile up for the test data yielded a faster operation for the fast channel, i.e. the pulse per resolution time was only about 1.57μs. The calculated and theoretical pile up curves are shown in Fig. 13.

The XSM front-end electronics is composed of the two different channels, both recording the same incoming photons. The fast channel acts as a photon counter. As long as the time interval between two successive incoming photons is greater than the pulse per resolution time, the fast channel can record all incoming photons. The other channel, the slow

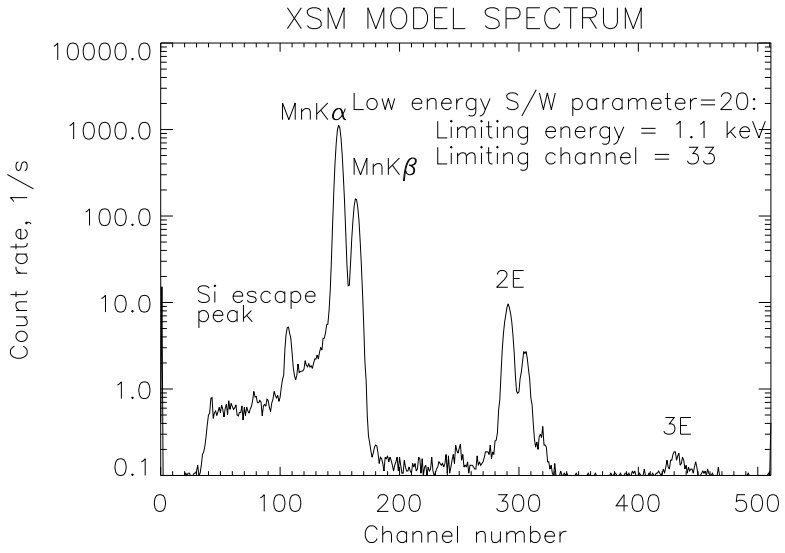

Figure 12.

channel, measures the energy of incoming photons. While a photon energy measurement is going on in the slow channel, this channel is closed for successive incoming photons. This means in practice, that all incoming photons are rejected, when a photon is under a pulse height measuring in the slow channel. The time period when the slow channel does not allow a new photon to enter the energy measuring process is called dead time. In a detector where is only one measuring channel, i.e. the slow channel, the lost signals due to dead time must be added to the measured signal using a Poisson statistical correction factor. This factor depends on the duration of the dead time and measured count rate. Using a fast channel readout to count the photons missed by the slow channel replaces the mathematical dead time correction, i.e. it acts as a "hardware dead time corrector". In this kind of a system there is no dead time. Another effect, pile up of the counts, cannot be avoided with any realistic solution, if the incoming photon count rate is very high.

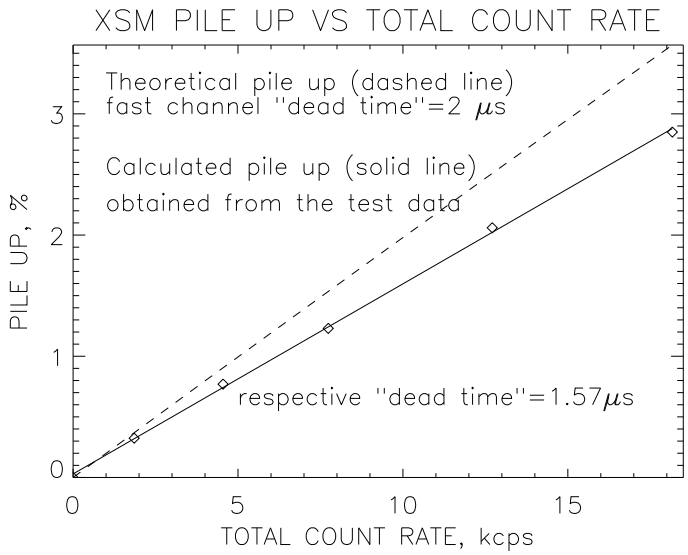

Figure 13.

2.6 Low energy threshold limit

The low energy limit determines the lowest applicable energy channel of the readout electronics. This limit can be changed and it is controlled by an on-board S/W parameter. The higher this limit, the higher the lowest energy recorded. If the detector is suffering from a low energy noise, the value of this limit can be adjusted higher to reduce the low energy noise. This value should be as low as possible, because the detector lower energy range depends on this value. If the value is set too low, the detector generates phantom counts. These excess counts are related to the interference with the fast channel operation. The aim of the loss free counting system is to add photons rejected by the slow channel into the final spectrum. The fast channel operation is very sensitive to any electrical interference. When the low energy threshold limit is set too low, the fast channel starts to generate phantom counts, which are added according to the loss free counting logic to the original spectrum so that the spectrum shape is preserved, but only the total intensity is increased. This kind of distortion effect is very difficult to recognize, and is therefore a potential source of serious scientific misinterpretations.

The aim of our tests were to find the lowest limit, at which the operation is stable, i.e. the low energy noise level is insignificant and the spectra are clean of phantom counts.

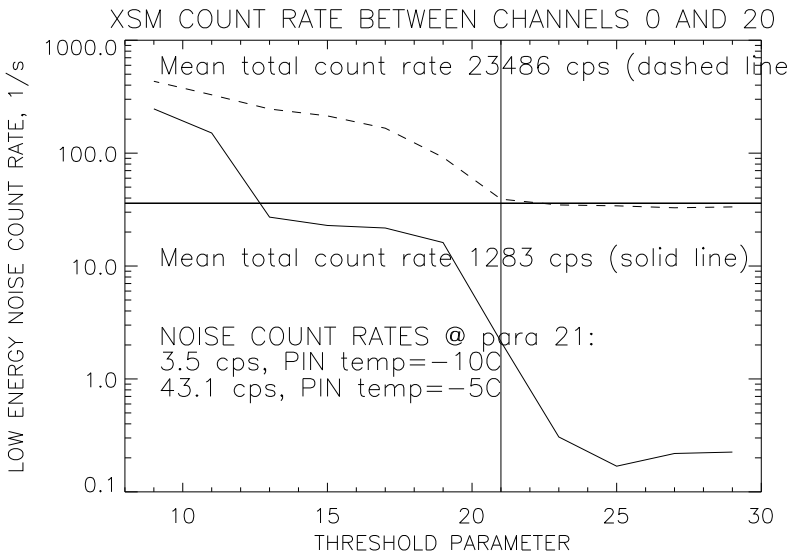

Figure 14.

We made several tests at OIA to find the optimal low energy limit for in-flight operation of XSM. These tests were made also with the FM electronics. Two test sequences were performed: One with a moderate count rate and the another with a high count rate. The radiation source was the same ^{55}Fe as used in the pile up test. In the first test run, the count rate was high and the operational PIN temperature was -5°C. The operational conditions could be regarded as 'hard' for XSM in this first test. Eleven integrations each containing about 10 spectra were taken at different values of the lower energy limit starting from the parameter value 9 and ending to the value 29. value 9 corresponds to an energy of 0.4 keV and 29 corresponds to an energy of 1.7 keV. The step interval was 2, i.e. only the odd values were included. The second test run was carried out with a moderate count rate and at a lower PIN temperature of -10°C corresponding to the 'nominal' operational conditions. Otherwise the second test was similar to the first test. The plot in Fig. 14 shows the low energy noise count rates as a function of the threshold parameter. The low and constant noise level starts at about 21 in both tests. Fig. 15 and Fig. 16 illustrate the total count rates as a function of the threshold parameter. It is clearly seen, that excess counts occur in the spectra, when the parameter is less than 21, i.e. loss free counting does not operate properly.

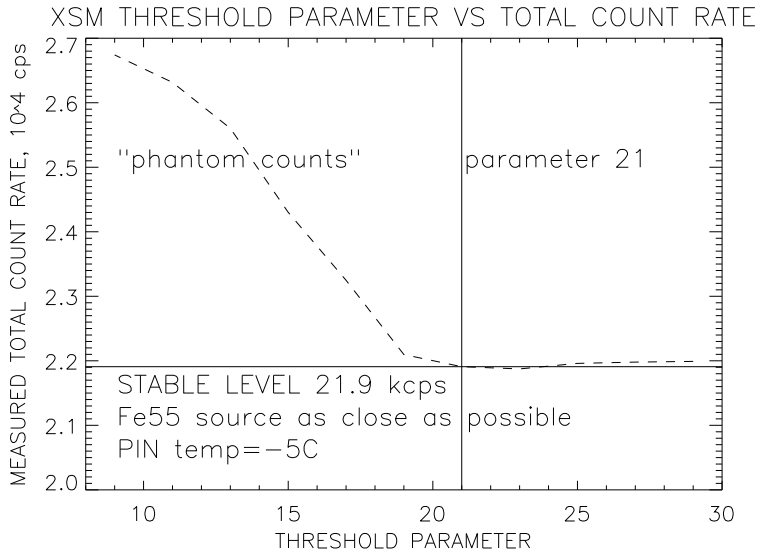

Figure 15.

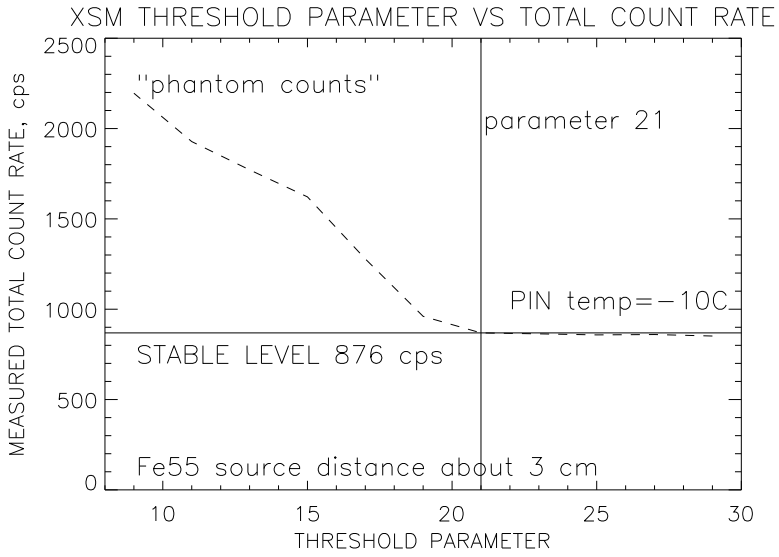

Figure 16.

The channel versus energy relation related to low energy threshold parameter values was also studied. All the spectra were analyzed by determining the lowest channel number containing at least a few counts. The lowest possibly recorded photon energy limits corresponding to the parameter limit values were derived by linear fitting. The line energies used in these fits were the Si escape peak (4.17 keV), Mn Kα (5.9 keV), Mn Kβ (6.5 keV) and *2E* pile up (11.9 keV). Hence, it was an easy task to determine the respective lowest possible channel energy corresponding to the low energy threshold parameter. The data points are plotted in Fig. 17. The fitted line in this figure represents the graph connect-

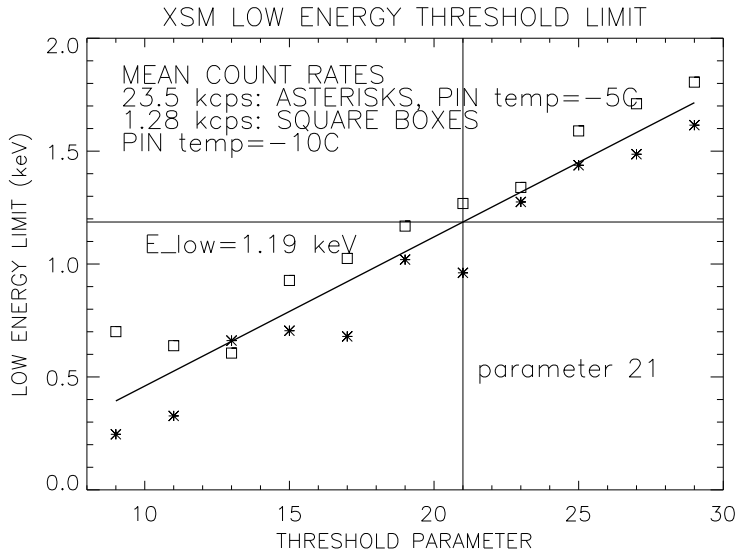

Figure 17.

ing the low energy threshold parameter and the lowest measurable photon energy. It is worthy of pointing out, that the gain and offset of XSM are also affected by the sensor box ambient temperature and detector PIN temperature.

2.7 Calibration with in-flight source

The in-flight calibration source is an ^{55}Fe plate attached on the shutter inner surface. This radiation source also contains a 5μm Ti-foil. Hence, the calibration spectrum contains four distinct emission line, which are Ti Kα at 4.5 keV, Ti Kβ at 4.9 keV, Mn Kα at 5.9 keV and Mn Kβ at 6.5 keV. It was found, that the source intrinsic intensity was low. The aperture stop hole is about 18 times smaller than it was in the SMART-1 XSM and the intrinsic source BoL (Begin of Life) intensities were the same. Hence, the calibration count rate was too low, yielding only about the count rate of 15 cps. With the aid of the fitted line centroids, we had to make tests about the required number of calibration spectra, which were needed to determine the gain and offset of XSM. The energy resolution was also investigated. The line centroids of Ti Kα and Mn Kα were be calculated to determine the channel versus energy relation. This required the summing

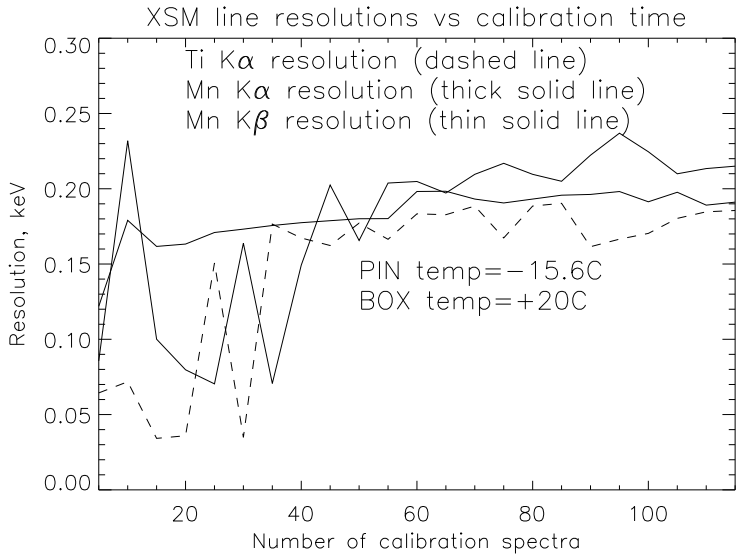

Figure 18.

of about 20 calibration spectra in total to get a sufficient photon statistics. The same amount of spectra was needed to determine the *FWHM* of the Mn Kα line. Due to the weakness of the Ti Kα line, the determination of the *FWHM* of Ti Kα line required far too many spectra of 16 seconds, i.e. spectra with too long integration time. The longer the calibration periods, the less solar data obtained. If the determination of the energy resolution of Ti Kα line failed for a sum of 20 spectra, the respective resolution could be determined iteratively. The method is introduced here in Eq. 2 and Eq. 3 below.

$$\Delta E \propto \sqrt{E} \tag{2}$$

$$\Delta E_1 = \Delta E_2 \sqrt{\frac{E_1}{E_2}} \tag{3}$$

The Gaussian fit tests of the three line energies are plotted in Fig. 18. The horizontal axis represents the number of added calibration spectra, which was required in the fitting of the energy resolutions. The parameter ΔE_1 denotes the resolution of the Ti Kα line, while ΔE_2 is the resolution of the Mn Kα line. The values for these were ΔE_1 =4.5 keV and ΔE_2=5.9 keV.

We have also studied the possibility to determine the detector offset and gain purely as a function of the detector PIN and sensor box temperature. Practically this means, that no in-flight calibration will be needed. The energy scale information associated to the RMF (Redistribution Matrix File) is taken from a table generated on the basis of ground calibrations.the before hand. This table includes the relation of the gain and offset as a function of the box temperature at a constant detector PIN temperatures. The PIN temperature can be stabilized with the aid of the Peltier cooler. Both of these temperature values with time stamps are part of the down linked telemetry data. As mentioned above, these two temperatures affect on the detector offset and gain, i.e. the determination of channel versus energy scale. We have made a fits describing the relation between the box temperature and gain at two constant PIN temperature of -9°C and -18°C. XSM performed a few long integrations with the shutter in closed position during the commissioning phase in November 2008. This calibration data were analyzed to determine the respective positions of line centroids of the TiKα and MnK α at several different sensor box temperatures. Those temperature were -15°C, -11°C, -3°C, 0°C and +4°C. The respective gain and offset values corresponding to the line centroids were calculated. The result of this analysis is shown in Fig. 19. The related numerical data is given in Table 7. The curves representing the fits are second degree polynomials. According to the 1σ error estimate, the confidence level of the above fits were quite low. The PIN temperature has been lowered down to -18°C after commissioning. Hence, we have to run several long calibrations at PIN temperature of -18°C to get sufficient data to repeat this analysis. We got same data for doing a respective preliminary analysis at a PIN temperature of -18°C. The results of this analysis are shown in Fig. 20.

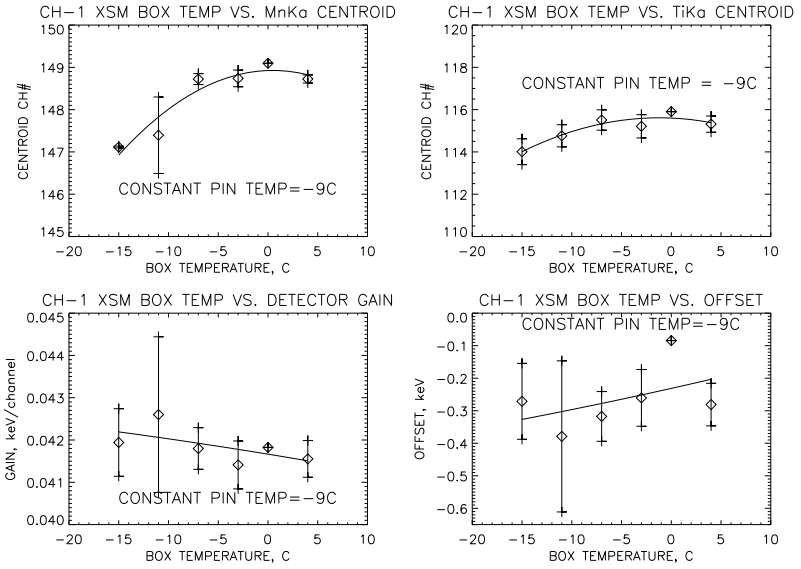

Figure 19.

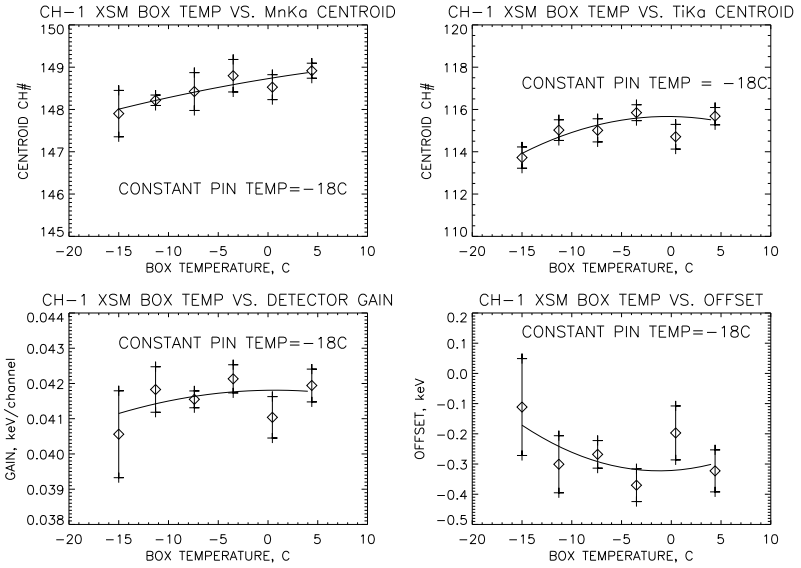

Figure 20.

3 In-flight operation

XSM performed several long calibration integrations during the commissioning phase. These spectra were clean of noise and the total calibration count rates were about 15 cps. The solar activity has been extremely low for a long period since the launch of Chandrayaan-1. Hence, the first data obtained with the shutter open contained only a few counts. We have done a test fitting for one solar observation on January. 10, 2009. The analyzed raw data spectrum is shown in Fig. 21. The fitting parameters are included

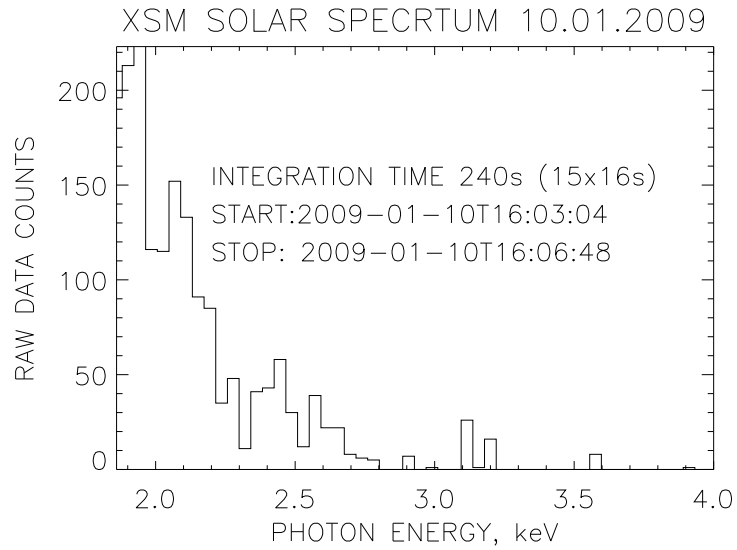

Figure 21.

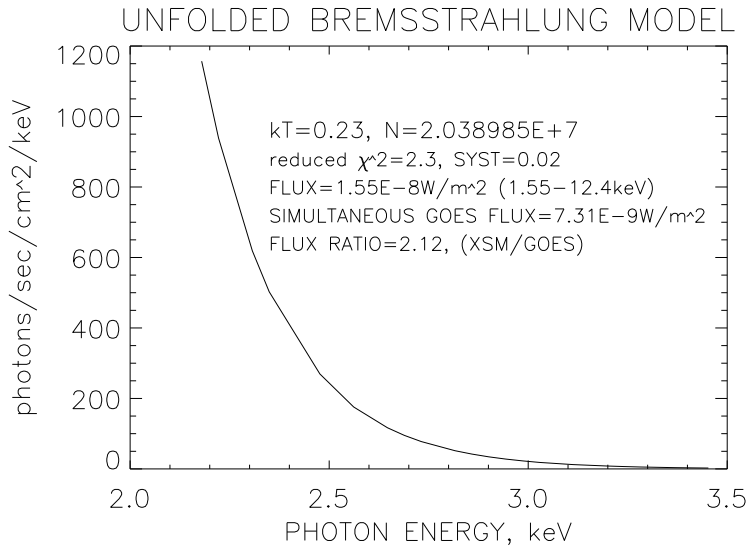

Figure 22.

in the plot shown in Fig. 22.

There is still some uncertainties in the operation of XSM. The background spectra seem to contain oddly distributed counts. There are only two or three random channels recording counts, but the number of counts per channel represent a count rate higher 5 cps, which is much too high for the real X-ray sky background emission. The rest of the channels were empty, excluding the first and the last channels. Some kind of phantom count phenomenon might be present. We will get a better estimate of the XSM perform-

ance as soon as the solar activity increases.

4 Conclusions

The ground calibrations of the Chandrayaan-1 XSM were carried out without problems. Hence, we expected to get high quality data from XSM during this lunar mission. According to the calibration data, XSM also worked well. During the low count rate observations, (i.e. off-solar pointings) XSM still recorded calibration counts even when the shutter is opened. The count rate level was only about 2/3 of that compared to the real calibration count rate. The phantom calibration spectra gradually faded away, after about ten spectra with the shutter open. This phenomenon was related to the FIFO/ASIC [6] operation, which is investigated further. The S/W parameter controlling the low energy threshold limit is set to 24 instead of the optimal value of 21. This present limit corresponds roughly to 1.4 keV according to the analysis in section 2.6.

One operational drawback was the annealing temperature, which was only +67°C instead of the desired +80°C. This was due to inappropriate design of the new power supply feeding the Peltier under the detector PIN. It simply supplies less power than required.

The accuracy related to derived fluxes is another open question. The example of the spectral analysis shown in the previous section did not match with the GOES data. XSM measured a twice greater simultaneous flux. We need to wait for the higher solar activity to verify the real performance and confidence of our new version of XSM.

5 Acknowledgments

These ground calibrations were supported by ESA funding.

We would also like to express our gratitude for the X-ray laboratory of the University

of Helsinki, which has been very flexible related to our work done at their laboratory. Special thanks go to the director of the X-ray laboratory Prof. Keijo Hämäläinen and the director of the Observatory Dr. Lauri Jetsu.

References

[1] Manuel Grande, et al., Current science, vol. 96, no. 4, 25 February 2009, The Chandrayaan-1 X-ray Spectrometer

[2] L. Alha, et al., Nuclear Instruments and Methods in Physics Research Section A: Accelerators, Spectrometers, Detectors and Associated Equipment, Volume 596, Issue 3, 11 November 2008, Pages 317-326, The in-flight performance of the X-ray Solar Monitor (XSM) on-board SMART-1

[3] H. Andersson, Personal communication with the representative of manufacturer (Oxford Instruments Analytical, former Metorex Inc., FIN).

[4] K. A. Arnaud,, 1996, Astronomical Data Analysis Software and Systems V, eds. Jacoby G. and Barnes J., p17, ASP Conf. Series volume 101.

[5] $http://www.ngdc.noaa.gov/stp/GOES/goes_1egend.htm$

[6] C. J. Howe, Personal communication with the representative of the FIFO/ASIC manufacturer (Rutherford Appleton Laboratory, Chilton, Didcot, OX11 OQX, UK)

Detector dimensions and performance	Nominal values
Detector thickness, Si	500.0 μm
Si dead layer thickness	0.01 μm
Al-filter+contact thickness , Al	0.60 μm
Polyimide filter	0.25 μm
Be-filter thickness	13.0 μm
Effective aperture stop diameter d_{det}	0.379 mm
Aperture diameter	4.70 mm
Detector-aperture distance	2.00 mm
Field of View cone angle radius	52°
Number of channels	512
Energy range	1.2 keV - 20.0 keV
Energy resolution (BOL)	200 eV at 6 keV
Pile up	3% at 20000 cps

Table 1

XSM filter and detector dimensions.

	Al Kα		Ca Kα		Ti Kα		Cu Kα			
Temp	cent	FWHM	cent	FWHM	cent	FWHM	cent	FWHM	gain	offset
+0°C	73.36	0.163	180.92	0.192	220.22	0.202	392.53	0.230	0.0206	-0.022
-5°C	72.60	0.180	179.80	0.176	219.30	0.191	390.87	0.219	0.0206	-0.012
-10°C	72.68	0.155	180.69	0.174	220.47	0.185	393.26	0.204	0.0205	-0.003
-15°C	72.10	0.151	179.91	0.174	219.39	0.181	392.20	0.197	0.0205	+0.008
-20°C	115.52	0.197	218.79	0.171	511.87	0.231	612.02	0.225	0.0206	-0.025

Table 2

Line centroids, energy resolutions, gains and offsets derived from the fluorescence lines of Al-CaCu powder mixture sample.

	Pb Mα		Ti Kα		Pb Lα		Pb Lβ			
Temp	cent	FWHM	cent	FWHM	cent	FWHM	cent	FWHM	gain	offset
+0°C	117.64	0.240	221.05	0.197	514.53	0.258	615.30	0.268	0.0206	-0.062
-5°C	117.42	0.220	221.55	0.196	516.28	0.251	617.16	0.254	0.0205	-0.051
-10°C	116.97	0.204	221.08	0.183	515.98	0.210	616.89	0.236	0.0205	-0.040
-15°C	116.15	0.204	220.09	0.184	514.41	0.233	615.39	0.216	0.0205	-0.026
-20°C	115.52	0.197	218.79	0.171	511.87	0.231	612.02	0.225	0.0206	-0.025

Table 3

Line centroids, energy resolutions, gains and offsets derived from the fluorescence lines of Pb plate sample.

source	Ti anode X-ray tube
tube voltage	12 keV
tube current	0.005 mA
slit size	10 mm x 10 mm
PIN temp	-15°C
chamber pressure	4 mbar
extra filters	4 capton foils
total count rate	3.0 kpcs
count rate (7-9 keV)	0.4 kcps
off-axis step	1°
number of steps per scan	111
number of scans	4
scan 1 roll angles	0°,...,180°
scan 2 roll angles	45°,...,225°
scan 3 roll angles	90°,...,270°
scan 4 roll angles	135°,...,315°

Table 4

The test setup parameters applied in the FoV sensitivity calibration.

	Chandrayaan-1 XSM FM	SMART-1 FS XSM
AlCaCu	three line+Ti Kα	three line+Ti Kα
PIN temp	-15°C	-15°C
Exposure time	3600 s	900 s
Chamber pressure	4mbar	4 mbar
Tube voltage	25 kV	25 keV
Tube current	0.5 mA	0.5 mA
Pb	three line+Ti Kα	three line+Ti Kα
PIN temp	-15°C	-15°C
Exposure time	3600 s	1800 s
Pressure	4mbar	4 mbar
Tube voltage	25 kV	25 keV
Tube current	0.5 mA	0.5 mA

Table 5

A list of comparison calibration test setup parameters.

Line energy, keV	K_{FM}	K_{FS}	K_{FM}/K_{FS}
Al Kα 1.487	220.2	219.9	0.998
Pb Mα 2.345	867.4	854.4	0.985
Ca Kα 3.692	673.2	659.1	0.979
Ti Kα 4.511	142.7	146,8	1,028
Cu Kα 8.047	1192.2	1206.3	1.012
Pb Lα 10.50	280.1	270.8	0.967
Pb Lβ 12.62	194.4	200.7	1.033

Table 6

Comparison calibration results between Chandrayyan-1 FM and SMART-1 FS XSM. Fitting parameters K_{FM} and K_{FS} are derived from the XSPEC S/W. Their dimension is photons/s/keV.

Box temp., °C	gain, keV/ch (-9°C)	offset, keV (-9°C)	gain, keV/ch (-18°C)	offset, keV (-18°C)
-15	0.041937557	-0.26796381	0.042192412	-0.32665113
-14	0.041901628	-0.27319130	0.042160418	-0.32075624
-13	0.041867759	-0.27797346	0.042127975	-0.31479539
-12	0.041835950	-0.28231028	0.042095081	-0.30876861
-11	0.041806199	-0.28620177	0.042061738	-0.30267587
-10	0.041778507	-0.28964793	0.042027945	-0.29651720
-9	0.041752875	-0.29264876	0.041993703	-0.29029257
-8	0.041729302	-0.29520425	0.041959010	-0.28400200
-7	0.041707788	-0.29731442	0.041923868	-0.27764549
-6	0.041688334	-0.29897925	0.041888276	-0.27122302
-5	0.041670938	-0.30019874	0.041852234	-0.26473462
-4	0.041655602	-0.30097291	0.041815742	-0.25818027
-3	0.041642325	-0.30130174	0.041778801	-0.25155997
-2	0.041631107	-0.30118524	0.041741409	-0.24487372
-1	0.041621948	-0.30062341	0.041703568	-0.23812153
0	0.041614849	-0.29961625	0.041665277	-0.23130340
+1	0.041609809	-0.29816375	0.041626536	-0.22441932
+2	0.041606828	-0.29626592	0.041587346	-0.21746929
+3	0.041605906	-0.29392276	0.041547706	-0.21045332
+4	0.041607043	-0.29113427	0.041507616	-0.20337140

Table 7

A table containing the numerical fit values for determining the gain and offset with the aid of

Fig. 1 XSM energy resolution as a function of photon energy at five different PIN temperatures.

Fig. 2 XSM FoV sensitivity map describing the obscuration factor.

Fig. 3 XSM roll angle directions related to the FoV sensitivity scanning.

Fig. 4 Aperture stop photographed with a microscope. Reference scale patterns are drawn in the figure.

Fig. 5 Pictures on the top row illusrtrate aperture stop holes in different pixel colours. (Plots are printed in black and white here.) Pictures in the lower row represennt the zoomed areas of the respective plots shown above.

Fig. 6 SMART-1 and CHANDRAYAAN-1 XSM Quantum efficiency curves.

Fig. 7 SMART-1 and CHANDRAYAAN-1 XSM effective area curves.

Fig. 8 XSM effective area plotted from 0° up to 53° at 1° steps.

Fig. 9 Fluorescence spectrum of the powder mixture of Al, Ca and Cu.

Fig. 10 Fluorescence spectrum of the Pb plate.

Fig. 11 Derived physical line intensity ratios.

Fig. 12 A model spectrum showing the lines used in the fit. The low energy S/W parameter was 20 during this pile up test corresponding to the lowest applicable channel number of 33 (=1.1 keV).

Fig. 13 Theoretical and derived pile up curves.

Fig. 14 XSM low energy noise as a function of threshold parameter at two different count rates.

Fig. 15 The measured count rate as a function of threshold parameter (high count rate).

Fig. 16 The measured count rate as a function of threshold parameter (moderate count rate).

Fig. 17 The low energy limit plotted as a function of the threshold parameter. The optimal parameter value 21 equals about 1.2 keV.

Fig. 18 Gaussian fitting routine applied on the three different lines. The resolutions stabilize after the total number of spectra used in fitting as about 60.

Fig. 19 XSM calibration line centroids, gain and offset fitted as a function of the box temperature at a constant PIN temperature of -9°C.

Fig. 20 XSM calibration line centroids, gain and offset fitted as a function of the box temperature at a constant PIN temperature of -18°C.

Fig. 21 XSM raw counts.

Fig. 22 Unfolded bremsstrahlung spectrum fitted with the XSPEC S/W.